Structural and Magnetic Investigation of Bi_2S_3@Fe_3O_4 Nanocomposites for Medical Applications

Ramazan Karaçam[1] · Nurdan Kurnaz Yetim[2] · Mümin Mehmet Koç[3] (ID)

Abstract

Bi_2S_3 and Fe_3O_4 nanostructures as well as Bi_2S_3@Fe_3O_4 nanocomposites were produced using hydrothermal synthesis. Scanning electron microscopy (SEM), energy dispersive spectra (EDS) and X-ray diffraction (XRD) were used in the characterization of the nanocomposites. The effect of heat treatment on chemical, physical and magnetic properties of the nanostructures was investigated in this study. It was determined that the duration of heat treatment affects the size and shape of the nanostructures. Bi_2S_3 samples produced using less than 12 h of heat treatment formed in nanoflower-like shapes whereas when the heat treatment was extended to 24 h, the samples formed in nanoribbon-like shapes. The study concludes that an increase in the duration of heat treatment enhances the saturation value of magnetization of Fe_3O_4 nanostructures. Bi_2S_3 nanostructures were doped with Fe_3O_4 nanostructures to produce Bi_2S_3@Fe_3O_4 nanocomposites which have significant magnetic properties. An increased duration of heat treatment increases the magnetic saturation values of Fe_3O_4 and Bi_2S_3@Fe_3O_4 nanostructures. Bi_2S_3, Fe_3O_4 and Bi_2S_3@Fe_3O_4 samples show X-ray imaging contrast enhancement properties.

Keywords Ferromagnetic nanoparticles · Bi_2S_3@Fe_3O_4 nanostructures · Bi_2S_3 nanoflowers · Nanocomposites · Magnetic properties · Bi_2S_3 nanoflowers

1 Introduction

Nanostructures have attracted attention in different fields such as physics, chemistry, material science and medical science and are used in many technological applications [1–3]. Nanomaterials are often considered a special phase between the bulk state and the atomic state. Chemical, physical and electronic properties of the nanomaterials may change depending on the size of the nanoparticles [4]. A size change in the nanostructures induces variation in the surface volume ratio of the materials which in turn affects the electronic properties and chemical and catalytic activity of the nanostructures [5, 6]. Various types of nanostructures such as nanotubes, nanowires and nanoparticles were reported in the literature [7–9].

Metallic nanostructures have an important place in sensor applications [10–15]. Metallic nanostructures have proven to significantly enhance the electronic and magnetic properties of thin films [16, 17]. For instance, using metal nanostructures in thin films applications such as photodetectors and sensors enhances device efficiency [18–20]. Each type of nanoparticle presents different properties. For example, Au and Bi nanoparticles show catalytic properties [21, 22] while CoO, GdO and FeO nanoparticles have ferromagnetic, antiferromagnetic and superparamagnetic properties [23–29]. Bi nanostructures show catalytic and photocatalytic properties with low bandgap energy that allows Bi nanostructures to be used in optoelectronic and thin film device applications [30, 31]. Moreover, Bi nanostructures are used in different types of medical applications. For example, Bi nanostructures have a high atomic number and high X-ray attenuation capacity; therefore, it has the potential to be used as an X-ray tomography contrast agent [2]. The surface of the Bi nanostructures could be modified and they can be targeted to a specific tissue and/or an organ [32, 33]. Bi_2S_3 nanostructures have also proven to have photothermal properties. Applying an 800-nm laser light on

✉ Mümin Mehmet Koç
muminmehmetkoc@klu.edu.tr

1 Department of Physics, Faculty of Arts and Sciences, Kırklareli University, Kırklareli, Turkey

2 Department of Chemistry, Faculty of Arts and Sciences, Kırklareli University, Kırklareli, Turkey

3 School of Medical Service, Kırklareli University, Kırklareli, Turkey

Bi_2S_3 nanostructures is found to increase the temperature of the nanoparticles. Liu et al. managed to visualize cancerous tissues and treat them using the photothermal therapy properties of Bi_2S_3 nanostructures [34].

Similar to Bi_2S_3 nanostructures, Fe_3O_4 nanostructures have potential medical applications. For instance, Fe_3O_4 nanostructures were reported as a potential MRI (Magnetic Resonance Imaging) contrast agent; the results reveal that they increased the MRI image quality [35–38]. Hyperthermia properties of the Fe_3O_4 nanostructures are well understood, and studies show that Fe_3O_4 nanostructures can be used as a multimodal contrast agent where both imaging and therapy properties can simultaneously be used [39–45]. Giving these observations in the previous studies, producing $Bi_2S_3@Fe_3O_4$ nanostructures may provide many benefits where nanoparticles showing high catalytic properties with magnetic properties may be obtained. Such nanoparticles may have MRI and X-ray computed tomography contrast properties with photothermal therapy and magnetic hyperthermia therapy properties. Using $Bi_2S_3@Fe_3O_4$ nanostructures in medical applications can help researchers to treat and visualize cancerous tissues simultaneously.

Prompted by the motivation above, we attempted to optimize the Bi_2S_3, Fe_3O_4 and $Bi_2S_3@Fe_3O_4$ nanostructures that were produced using the hydrothermal method (Table 1). We investigated the production parameters of morphological, structural and magnetic properties of Bi_2S_3, Fe_3O_4 and $Bi_2S_3@Fe_3O_4$ nanostructures (Table 1). It was found that the increased heat treatment alters the morphological structures of Fe_3O_4 and Bi_2S_3 nanostructures (Fig. 1) and increased the

ferromagnetic properties of Fe_3O_4 and $Bi_2S_3@Fe_3O_4$ nanostructures.

2 Materials and Methods

2.1 General Chemicals

All chemicals used in the experiments were of analytical grade; they were used without any further purification. Bismuth nitrate pentahydrate ($Bi(NO_3)_3.5H_2O$), thiourea (CH_4N_2S), Iron(II) sulfate heptahydrate ($FeSO_4.7H_2O$) and sodium hydroxide (NaOH) were purchased from Sigma-Aldrich. Deionized water (DI) with a resistance of 18.25 MΩ was used in all experiments.

2.2 Sample Preparation

2.2.1 Synthesis of Magnetic Micro/Nano Fe_3O_4 Particles

Magnetic nanoparticles were synthesized using a hydrothermal synthesis approach. A total of 0.656 g of $FeSO_4.7H_2O$ was dissolved in 40 mL of deionized water, and 3.2 g of NaOH was then added to the solution. This solution was stirred for 10 min and then transferred into a 50 mL stainless steel–coated Teflon-lined autoclave. This Teflon-lined autoclave was then placed in a conventional oven and heated at 150 °C for 24 h. The resulting black precipitate was collected by centrifugation at 8000 rpm for 20 min and washed several times with deionized water and absolute ethanol. The solid

Table 1 Structure shape and saturation magnetization values of samples regarding the preparation conditions

| Materials	Reactant	Medium	Reaction time/temperature	Structure	Saturated magnetization value (emu/g)
$(Fe_3O_4)_{1h}$	$FeSO_4.7H_2O$; NaOH	D.I	1 h/150 °C	Nanospheres	18.4
$(Fe_3O_4)_{12h}$	$FeSO_4.7H_2O$; NaOH	D.I	12 h/150 °C	Nanospheres	87.7
$(Fe_3O_4)_{24h}$	$FeSO_4.7H_2O$; NaOH	D.I	24 h/150 °C	Nanospheres	90.4
$(Bi_2S_3)_{12h}$	$Bi(NO_3)_3.5H_2O$; CH_4N_2S	D.I	12 h/150 °C	Nanoflower	-
$(Bi_2S_3)_{24h}$	$Bi(NO_3)_3.5H_2O$; CH_4N_2S	D.I	24 h/150 °C	Nanoribbon	-
$(Bi_2S_3)_{12h}@(Fe_3O_4)_{1h}$	$Bi(NO_3)_3.5H_2O$; (CH_4N_2S); $FeSO_4.7H_2O$; NaOH	D.I	1 h/150 °C	Nanoflower	2.24
$(Bi_2S_3)_{12h}@(Fe_3O_4)_{12h}$	$Bi(NO_3)_3.5H_2O$; CH_4N_2S; $FeSO_4.7H_2O$; NaOH	D.I	12 h/150 °C	Nanoflower	3.73
$(Bi_2S_3)_{12h}@(Fe_3O_4)_{24h}$	$Bi(NO_3)_3.5H_2O$; CH_4N_2S; $FeSO_4.7H_2O$; NaOH	D.I	24 h/150 °C	Nanoribbon	12.6
$(Bi_2S_3)_{24h}@(Fe_3O_4)_{1h}$	$Bi(NO_3)_3.5H_2O$; CH_4N_2S; $FeSO_4.7H_2O$; NaOH	D.I	1 h/150 °C	Nanoribbon	2.67
$(Bi_2S_3)_{24h}@(Fe_3O_4)_{12h}$	$Bi(NO_3)_3.5H_2O$; CH_4N_2S; $FeSO_4.7H_2O$; NaOH	D.I	12 h/150 °C	Nanoribbon	18.6
$(Bi_2S_3)_{24h}@(Fe_3O_4)_{24h}$	$Bi(NO_3)_3.5H_2O$; CH_4N_2S; $FeSO_4.7H_2O$; NaOH	D.I	24 h/150 °C	Nanoribbon	22.5

D.I deionized water
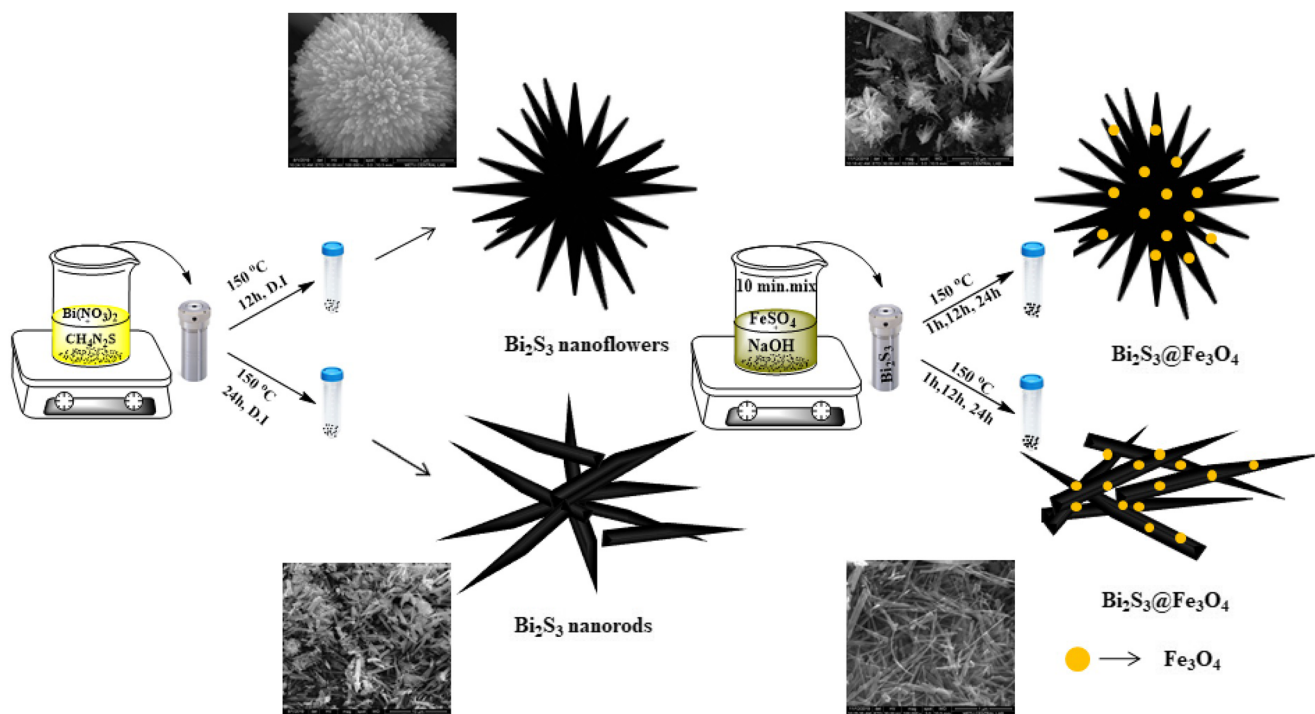
Fig. 1 Schematic representation of the synthesis of Bi$_2$S$_3$ nanoflower and nanorod and Bi$_2$S$_3$ @ Fe$_3$O$_4$ nanostructures

was placed in a vacuum oven at 40 °C for 1 h [46]. The same procedure was repeated in a stainless steel–coated Teflon-lined autoclave and heated to 150 °C for 6 and12 h.

2.2.2 Synthesis of Micro/Nano Bi$_2$S$_3$ Structures

For the synthesis of Bi$_2$S$_3$ nanoparticles, after dissolving 0.25 g of thiourea in 40 mL of deionized water, 0.61 g of Bi(NO$_3$)$_2$.5H$_2$O was added. The solution was stirred while at a termperature of 60 °C for 20 min on a magnetic stirrer. The solution was transferred into a 40 mL stainless steel–coated Teflon-lined autoclave and heated to 150 °C for 12 h. The resulting black precipitate was collected by centrifugation at 8000 rpm for 20 min and washed several times with deionized water and absolute ethanol. The precipitate was stored at 80 °C for 24 h [47, 48]. The same process was repeated in a stainless steel–coated Teflon-lined autoclave and kept at 150 °C for 24 h.

2.2.3 Synthesis of Magnetic Bi$_2$S$_3$@Fe$_3$O$_4$

A total of 0.2 g of Bi$_2$S$_3$ (obtained after 12 and 24 h) was dispersed in 20 mL of deionized water in an ultrasonic bath. In a separate beaker, 0.332 g of FeSO$_4$.7H$_2$O was dissolved in 20 mL of deionized water. A total of 1.6 g of NaOH was then added to the solution and stirred for 10 min. The prepared solution was then poured onto Bi$_2$S$_3$. This mixture was stirred in an ultrasonic bath for a further 5 min in a stainless steel–

coated 40 mL capacity Teflon-lined autoclave, was taken and kept at 150 °C for 1 h. The resulting black precipitate was collected by centrifugation at 8000 rpm for 20 min and washed several times with deionized water and absolute ethanol. The precipitate was placed in an oven at 80 °C for 24 h. The same procedure was repeated in stainless steel–coated Teflon autoclave and kept at 150 °C for 12 and 24 h.

2.3 Characterization

X-ray diffraction (XRD) patterns were obtained on a RİGAKU miniflex600 X-ray diffractometer equipped with Ni-filtered Cu Kα source at a scan range of $10 < 2\theta < 90$. The infrared spectrum was recorded by a JASCO FTIR-6700 spectrometer between wavelengths of 400 to 4000 cm^{-1}. The surface morphology of nanostructures was also investigated using scanning electron microscopy (SEM). SEM–energy dispersive X-ray spectroscopy (EDX) analysis was performed on FEI Quanta 400F model device, and the profiles were used to determine the elemental composition. HR-TEM (high-resolution transmission electron microscopy) studies were carried out on a Jeol 2100F electron microscope at an acceleration voltage of 200 kV. Magnetic measurements were performed at room temperature using a vibrating sample magnetometer, Cryogenic Limited PPMS, with the maximum magnetic field of ± 1 Tesla. A medical-type X-ray imaging system was used in the assessment of the contrast properties of the samples.

3 Results and Discussion

3.1 Phase Composition and Morphology of Samples (XRD)

To assess the physical and crystal properties of the samples, X-ray diffraction method was used. X-ray diffraction patterns of Fe_3O_4(**a**), Bi_2S_3(**b**) and $Bi_2S_3@Fe_3O_4$(**c**) nanostructures are presented in Fig. 2. In Fig. 2a, b and c, all crystal orientations observed for Fe_3O_4, Bi_2S_3 and $Bi_2S_3@Fe_3O_4$ samples were tagged upon each peak. The detailed structural formation of the samples is given as follows. Figure 2a illustrates the XRD pattern of Fe_3O_4 nanostructures where a distinctive peak was observed at 35.6°, 30.4° and 62.8°. The peak indicates the existence of (311), (220) and (400) face-centred cubic (fcc) crystal orientation of Fe_3O_4 structure which shows good accordance with the previous results reported by Zhu et al. [49]. Overall, peaks at 18.3°, 30.4°, 35.6°, 37.08°, 43.3°, 53.36°, 57.3°, 62.8°, 70.98°, 74.12°, 74.98° and 78.94° were observed which indicates (1 1 1), (2 2 0), (3 1 1), (2 2 2), (4 0 0), (4 2 2), (5 1 1), (4 4 0), (6 2 0), (5 3 3), (6 2 2) and (4 4 4) structure formation [46, 50, 51].

Figure 2b illustrates XRD patterns of Bi_2S_3 nanostructures which were produced in 24 h and 12 h, respectively. Both Bi_2S_3-24 h and Bi_2S_3-12 h have almost identical X-ray patterns. Similar XRD patterns indicate that both Bi_2S_3-12 h and Bi_2S_3-24 h samples have the same chemical form and same crystal order. Two distinctive peaks were obtained for Bi_2S_3-12 h and Bi_2S_3-24 h samples for 25.07° and 28.67° which indicate the orthorhombic structure at (111) and (230) orientations, respectively. Overall, peaks observed at 15.74°, 17.65°, 22.44°, 23.74°, 25.07°, 27.42°, 28.67°, 31.86°, 32.7°, 33.96°, 35.69°, 36.61°, 39.13°, 40.06°, 42.69°, 45.60°, 46.60°, 48.38°, 49.16°, 51.41°, 52.71°, 52.92°, 54.67° and 59.29° that illustrate the existence of orthorhombic formation at (0 2 0), (1 2 0), (2 2 0), (1 0 1), (1 1 1), (0 2 1), (2 3 0), (2 2 1), (3 0 1), (3 1 1), (2 4 0), (2 3 1), (0 4 1), (1 4 1), (4 2 1), (0 0 2), (4 3 1), (0 6 0), (2 5 1), (2 2 2), (3 1 2), (0 6 1), (2 3 2) and (6 4 0) orientations, respectively [48, 52].

Figure 2c illustrates the XRD pattern of $Bi_2S_3@Fe_3O_4$ sample. The $Bi_2S_3@Fe_3O_4$ sample was produced by doping Bi_2S_3 nanostructures with Fe_3O_4 nanostructures. To assess the alteration in the nanostructure after the doping mechanism, both Bi_2S_3 and Fe_3O_4 XRD patterns were presented along
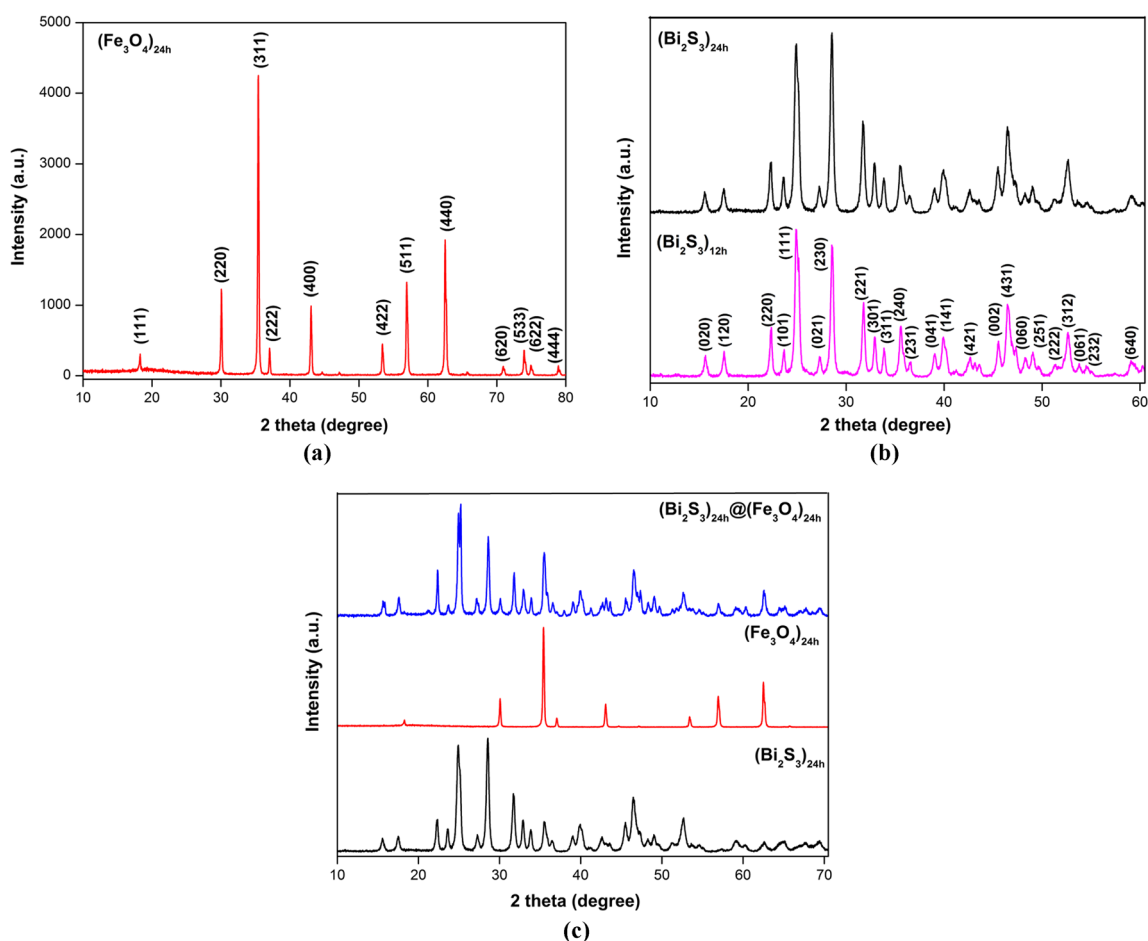

Fig. 2 XRD patterns of Fe_3O_4 (**a**), Bi_2S_3 (**b**) and $Bi_2S_3@Fe_3O_4$ (**c**) samples

with the XRD patterns of Bi_2S_3@Fe_3O_4. It was observed that the XRD pattern of Bi_2S_3@Fe_3O_4 nanostructures consists of a combination of XRD patterns of Bi_2S_3 and Fe_3O_4 nanostructures where Bi_2S_3 and Fe_3O_4 patterns overlapped. The observed peaks of both XRD patterns of Bi_2S_3 and of Fe_3O_4 were also identified in the XRD patterns of Bi_2S_3@Fe_3O_4. XRD patterns of the Bi_2S_3@Fe_3O_4 structures indicate that chemical structures of Bi_2S_3 and Fe_3O_4 nanostructures were not changed after doping. Therefore, it reveals that Fe_3O_4 nanostructures were physically doped on Bi_2S_3 nanoparticles. It is highly possible that Bi_2S_3 and Fe_3O_4 nanostructures were formed as a composite structure in Bi_2S_3@Fe_3O_4 nanostructures. TEM and SEM images also confirm that physical doping of Fe_3O_4 on Bi_2S_3 nanostructures occurred.

3.2 Morphology and Structure (SEM-EDX, HR-TEM)

Morphology and physical structure of the Bi_2S_3, Fe_3O_4 and Bi_2S_3@Fe_3O_4 nanostructures were assessed using microscopic methods. SEM was used as a primary tool for microscopic investigation while HR-TEM was utilized to investigate the structural properties of the samples. SEM images reveal that $(Fe_3O_4)_{1h}$ and $(Fe_3O_4)_{12h}$ nanostructures were formed in nano-size and mostly spherical form. TEM image of $(Fe_3O_4)_{1h}$ was also presented in Fig. 3d and reveals that the size of the $(Fe_3O_4)_{1h}$ nanoparticles was found to be less than 10 nm where the nanoparticles formed a stacked lump. The size of $(Fe_3O_4)_{24h}$ nanoparticles was found to be in nanocube form which is larger than that of $(Fe_3O_4)_{1h}$ and $(Fe_3O_4)_{12h}$ nanoparticles. SEM and TEM images reveal that nanoparticles constituting the Fe_3O_4 samples possess a narrow size distribution. However, it was observed that nanoparticles stack on each other resulting in producing big agglomerates where the size of agglomerates may reach up to 1 μm. Therefore, the increased thermal treatment duration results in increased agglomeration and size. TEM results confirm that such agglomerates consist of smaller Fe_3O_4 nanoparticles which are smaller than 100 nm.

EDS results confirm that Fe_3O_4 nanoparticles were consisting of Fe and O molecules where no contamination was observed in the structure. SEM investigations of Bi_2S_3 samples reveal that Bi_2S_3 samples show two different formations: nanoflowers (*i*) and nanorods (*ii*). Nanoflowers were observed in the Bi_2S_3 samples that received heat the treatment for less than 12 h. On the other hand, Bi_2S_3 having heat treatment more than 12 h gradually loses the flower-like formations where fibre and/or ribbon like formations were observed. $(Bi_2S_3)_{12h}$ samples consist of nanoribbons and its thickness is less than 60 nm and agglomerated in a special form. Such an agglomeration forms a flower-like shape where increased surface volume ratio was obtained for the $(Bi_2S_3)_{12h}$ structures. The thickness of the nanorods in nanoflowers was found to be less than 60 nm while the length of each rode in nanoflower can reach up to 1 μm. SEM images reveal that $(Bi_2S_3)_{24h}$ samples were formed in nanoribbon form where stacked ribbon like stripes can be seen in the figures. It was understood that the increased heat treatment causes an alteration in the morphological structure of the nanoparticles where the shape was deformed. The ribbon-like structures which were forming the flower-like shape were individually observed. With the increased heat treatment, the size of the rods increases and forms as nanoribbon-like fibres. The thickness of the ribbons was found to be about 200 nm while the length of the ribbons may reach up to a couple of micrometres. EDS results confirm the exitance of Bi and S molecules in Bi_2S_3 nanostructures where no contamination peak was observed in the nanoparticles.

SEM images of $(Bi_2S_3)_{24h}$@$(Fe_3O_4)_{24h}$ nanostructures were presented in Fig. 4. Further evidence from the images confirms that the increased heat treatment decomposes the flower-like structure. Flower-like structures have a high surface volume ratio. Heat treatment may change their thermodynamic instability. Therefore, the nanoflower form may be decomposed and nanoribbon-nanofibre-like structures can be seen in the images. The thickness of the nanoribbon-like structure was found to be less than 100 nm. The length of the nanoribbons changes which may reach up to a couple of micrometres. It was confirmed by the microscopy images that the increased heat treatment also increases the length of the nanoribbons. EDS results confirm the existence of Fe, O, Bi and S elements in the nanostructures which indicate that Fe nanostructures were successfully doped on Bi_2S_3 nanostructures. Moreover, TEM images confirm the stripy shape of Bi_2S_3 nanostructures where Fe_2O_3 nanoparticles could be identified. It was understood from the TEM images of $(Bi_2S_3)_{24h}$@$(Fe_3O_4)_{24h}$ that $(Bi_2S_3)_{24h}$ and $(Fe_3O_4)_{24h}$ physically united with the heat treatment. XRD analysis shows that both Fe_3O_4 and Bi_2S_3 nanostructures retain their crystal form which demonstrates that $(Bi_2S_3)_{24h}$@$(Fe_3O_4)_{24h}$ was formed in nanocomposite form. The heterogeneous colour difference in the structure of the $(Bi_2S_3)_{24h}$@$(Fe_3O_4)_{24h}$ can be seen in the TEM images providing further evidence of nanocomposite formation.

SEM images of $(Bi_2S_3)_{12h}$@$(Fe_3O_4)_{1h}$ and $(Bi_2S_3)_{24h}$@$(Fe_3O_4)_{1h}$ samples and element-based EDS mapping results were presented in Fig. 5. It was observed in SEM images that the flower-like form of Bi_2S_3 in $(Bi_2S_3)_{12h}$@$(Fe_3O_4)_{1h}$ was sustained. This confirms that Fe_3O_4 nanoparticles were stacked between the nanoribbons which give flower form to Bi_2S_3 nanostructures. Since the size of $(Fe_3O_4)_{1h}$ structures was found to be relatively smaller than other Fe_3O_4 samples, it is more likely to have the formation of a coating shell over the nanoflower-like structures in such nanoparticles. Moreover, Bi_2S_3 nanostructures which constitute $(Bi_2S_3)_{24h}$@$(Fe_3O_4)_{1h}$ were formed as nanoribbons. Bi_2S_3 nanoribbons were found to be accumulated randomly
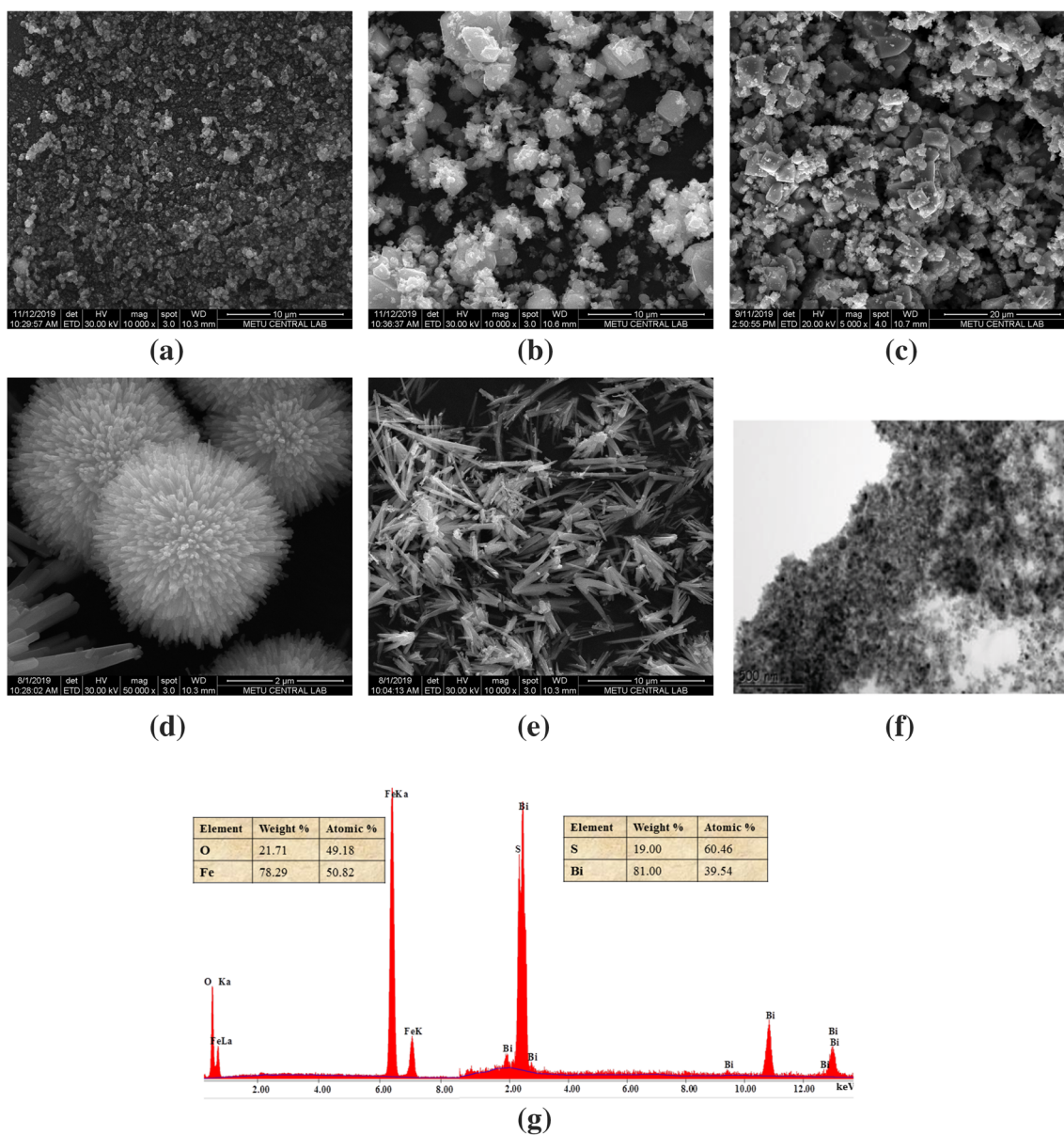
Fig. 3 SEM images of $(Fe_3O_4)_{1h}$ (**a**), $(Fe_3O_4)_{12h}$ (**b**), $(Fe_3O_4)_{24h}$ (**c**), $(Bi_2S_3)_{12h}$ (**d**) and $(Bi_2S_3)_{24h}$ (**e**); TEM images of $(Fe_3O_4)_{1h}$ (**f**); and EDX spectrum of Fe_3O_4, Bi_2S_3 (**g**) nanostructures

where Fe_3O_4 nanostructures were stacked on them. Since the size of the Fe_3O_4 nanoparticles was very low compared with the size of the Bi_2S_3 nanoribbons, their visualization was found to be difficult. However, elemental EDS mapping confirms the exitance of Fe and O structures in the $(Bi_2S_3)_{24h}@(Fe_3O_4)_{1h}$ samples.

3.3 Magnetic Properties of the Fe_3O_4 and $Bi_2S_3@Fe_3O_4$ Nanostructures (VSM)

Bi_2S_3 nanostructures were observed to show good photothermal and photocatalysis properties. Such structures do not exhibit a ferromagnetic property. Vibrating sample magnetometry (VSM) is often used to assess the ferromagnetic properties of the materials. There is no paper in the literature that illustrates that Bi_2S_3 structures show ferromagnetic properties. Therefore, magnetic properties of Bi_2S_3 structures were not assessed using VSM. Magnetic properties of the Fe_3O_4 and $Bi_2S_3@Fe_3O_4$ nanostructures were investigated using VSM, and the results are presented in Fig. 6. VSM assessments give information about the magnetic properties of the nanoparticles. Magnetic response of Fe_3O_4 and $Bi_2S_3@Fe_3O_4$ nanostructures produces hysteresis curves, which indicates that Fe_3O_4 and $Bi_2S_3@Fe_3O_4$ nanostructures reflect

Fig. 4 TEM images (**a** and **b**) and EDS spectra (**c**) of $Bi_2S_3@Fe_3O_4$ magnetic nanostructures

Element	Weight %	Atomic %
O	15.41	39.54
S	4.78	6.12
Fe	28.17	20.71
Bi	44.35	8.71
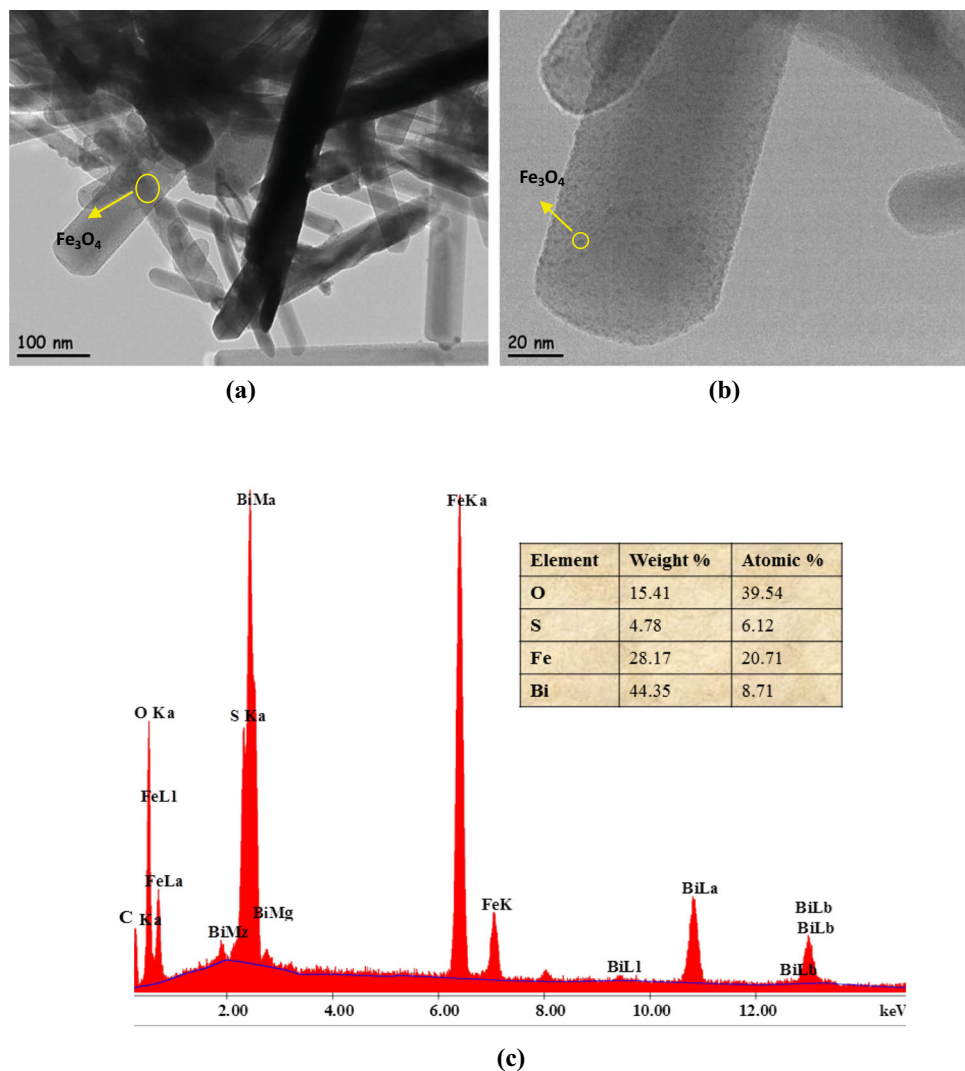
ferromagnetic properties. Figure 6a shows the magnetic behaviours of Fe_3O_4 nanostructures. The lowest magnetic saturation is obtained for $(Fe_3O_4)_{1h}$ sample which is 18.4 emu/g. Increased saturation was obtained for the increased heat treatment where 87.7 and 90.4 emu/g were obtained for $(Fe_3O_4)_{12h}$ and $(Fe_3O_4)_{24h}$, respectively. It was observed that our nanostructures have higher magnetic saturation values than that of results reported in the literature. For example, Zhu et al. reported maximum magnetic saturation values of 66.5 emu/g for Fe_3O_4. The thickness of the hysteresis curves indicates that $(Fe_3O_4)_{1h}$ shows harder magnetic behaviour than other (Fe_3O_4) samples, since the curve reveals thicker characteristics [53]. It concludes that $(Fe_3O_4)_{1h}$ sample has harder ferromagnetic properties.

It was previously mentioned that increased heat treatment increases the particle size of Fe_3O_4 nanostructures, which alters the surface volume ratio. The increases in size may help to form bigger domains and therefore increase the saturation values of Fe_3O_4 nanostructures

[54]. Size-related magnetic behaviours of nanoparticles were previously reported [55, 56]. Therefore, results show coherence with the previously reported results in the literature. Figure 6b and c show VSM results of $Bi_2S_3@Fe_3O_4$ nanostructures. Originally, Bi_2S_3 does not possess a ferromagnetic property. However, Fig. 6b and c show the hysteresis curves, which confirm that $Bi_2S_3@Fe_3O_4$ structures have ferromagnetic properties. Similar cases were also reported in the literature [50, 57]. Graphs indicate that doping the Bi_2S_3 with Fe_3O_4 nanoparticles alters the magnetic properties of the Bi_2S_3 nanostructures and gives Bi_2S_3 nanostructure ferromagnetic properties.

In Fig. 6b, saturation values were found to be 2.24 emu/g, 3.73 emu/g and 12.6 emu/g for $(Bi_2S_3)_{12h}@(Fe_3O_4)_{1h}$, $(Bi_2S_3)_{12h}@(Fe_3O_4)_{12h}$ and $(Bi_2S_3)_{12h}@(Fe_3O_4)_{24h}$, respectively. It was understood that the increased heat treatment increases the ferromagnetic saturation values. The results also support the size-related scenario of the Fe_3O_4 nanostructures
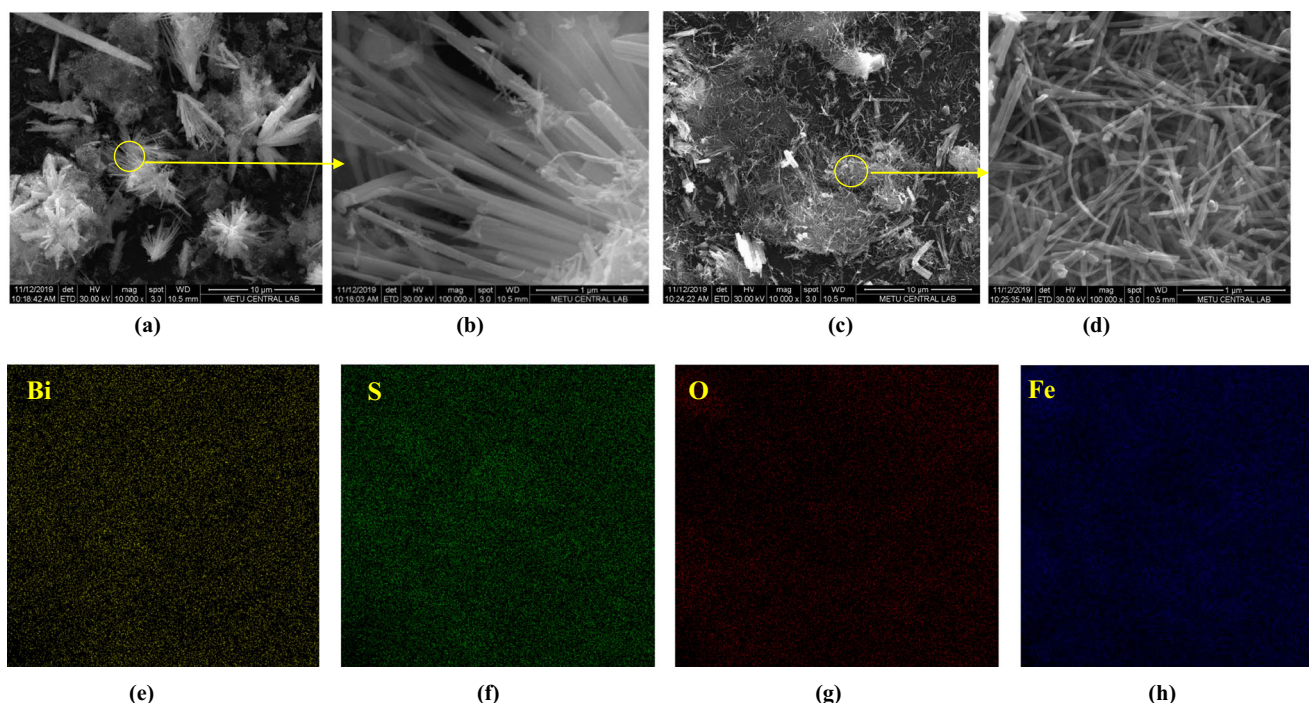
Fig. 5 SEM images of $(Bi_2S_3)_{12h}@(Fe_3O_4)_{1h}$ (**a** and **b**) and $(Bi_2S_3)_{24h}@(Fe_3O_4)_{1h}$ (**c** and **d**) nanostructures. Elemental maps of nanostructures were presented below the SEM image of $Bi_2S_3@Fe_3O_4$ sample where Bismuth (Bi) (**e**), Sulphur (S) (**f**), Oxygen (O) (**g**) and Iron (Fe) (**h**) maps were presented

where increased size may result in increased domain area [54]. Increased domain size increases the area of magnetic moments that enhances the magnetic saturation limits. Figure 6c illustrates the magnetic behaviours of $(Bi_2S_3)_{24h}@(Fe_3O_4)_{1h}$, $(Bi_2S_3)_{24h}@(Fe_3O_4)_{12h}$ and $(Bi_2S_3)_{24h}@(Fe_3O_4)_{24h}$, respectively. Magnetic saturation values were found to be 2.67 emu/g, 22.5 emu/g and 28.6 emu/g, for $(Bi_2S_3)_{24h}@(Fe_3O_4)_{1h}$, $(Bi_2S_3)_{24h}@(Fe_3O_4)_{12h}$ and $(Bi_2S_3)_{24h}@(Fe_3O_4)_{24h}$, respectively. Results presented in Fig. 6c were found to be parallel to the results presented in Fig. 6a and Fig. 6b. Similarly, the increased heat treatment results in the increased saturation values which may depend on the increased domain size. Moreover, saturation values presented for $(Bi_2S_3)_{24h}$ samples were found to higher than that of the results presented for $(Bi_2S_3)_{12h}$. It was previously reported that the increased thermal treatment decomposes the

flower-like structure and forms nanoribbon-like structures. $Bi_2S_3@Fe_3O_4$ nanocomposites reflect higher magnetic saturation values than that of values reported in the literature. For example, Zhu et al. reported 0.65 emu/g for their $Bi_2S_3@Fe_3O_4$ nanostructures which is much lower than our results [49].

At this point, doping different types of nanostructures with Fe_3O_4 will provide various ferromagnetic properties. It is possible that the structure of the nanoflower will enable Fe_3O_4 nanostructures to be doped inside the nanoflowers since surface volume ratio of the flower-like structures is much higher than nanoribbons [54]. On the other hand, in the doping process of Bi_2S_3 nanoribbon with Fe_3O_4 nanoparticles, most of the Fe_3O_4 nanoparticles will be doped on the surface of the nanoribbons. Therefore, bigger Fe_3O_4 domains can be formed on the surface of Bi_2S_3 nanoribbon which will give rise to
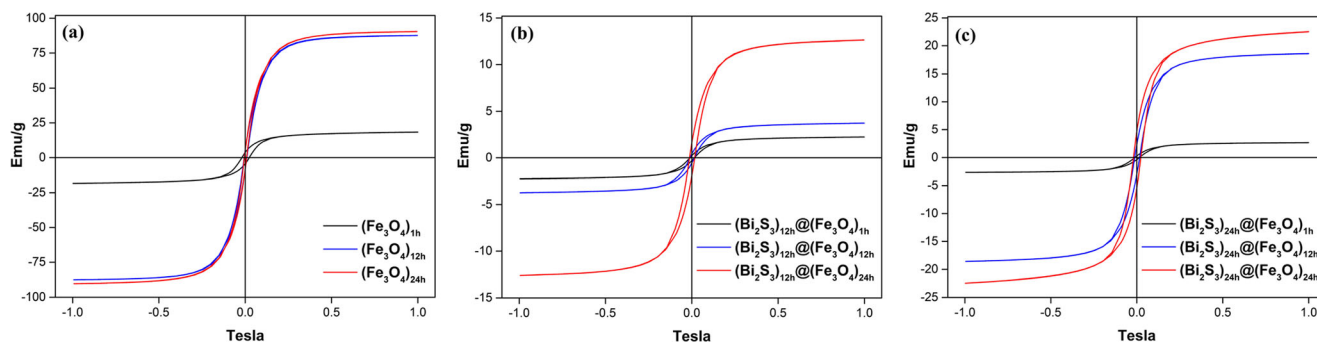

Fig. 6 Magnetic hysteresis of (**a**) Fe_3O_4 and $Bi_2S_3@Fe_3O_4$ (**b** and **c**) nanostructures

higher magnetic saturation values than that of flower-like formations. The structural difference affects the ferromagnetic characteristics of the samples.

3.4 X-Ray Imaging Contrast Enhancement Properties of Bi_2S_3, Fe_3O_4 and $Bi_2S_3@Fe_3O_4$ Nanostructures

Bi_2S_3 nanoparticles have the potential to be used as X-ray computed tomography contrast agents. Since the aim of this work is to produce nanoparticles that can potentially be used in medical applications, we investigate the X-ray computed tomography contrast enhancement properties of nanoparticles (Fig. 7). To study the contrast enhancement properties properly, empty (1), water filled (2), $(Fe_3O_4)_{24h}$ + water (3), $(Bi_2S_3)_{24h}$ + water (4) and $(Bi_2S_3)_{24h}@(Fe_3O_4)_{24h}$ + water (5) Eppendorf tubes were prepared, and an X-ray imaging procedure was performed. The highest contrast was obtained for $(Bi_2S_3)_{24h}$ which confirms that Bi_2S_3 nanoparticles have contrast enhancement properties (Fig. 7). Visual inspection confirms that $(Bi_2S_3)_{24h}@(Fe_3O_4)_{24h}$ nanocomposite shows a good contrast enhancement but not as good as the pure $(Bi_2S_3)_{24h}$ sample. $(Fe_3O_4)_{24h}$ nanoparticles also show contrast enhancement properties where $(Fe_3O_4)_{24h}$ sample gives better contrast enhancement than water (2) and air (1) sample. Visual inspection reveals that $(Bi_2S_3)_{24h}$ gives the best contrast enhancement which was slightly better than the contrast enhancement of $(Bi_2S_3)_{24h}@(Fe_3O_4)_{24h}$. Such a result indicates that doping $(Bi_2S_3)_{24h}$ with $(Fe_3O_4)_{24h}$ samples decreases the contrast enhancement properties of the nanocomposite where $(Fe_3O_4)_{24h}$ nanoparticles do not have as high contrast enhancement properties as $(Bi_2S_3)_{24h}$.

4 Conclusions

Bi_2S_3, Fe_3O_4 and $Bi_2S_3@Fe_3O_4$ samples were successfully produced using the hydrothermal method. Chemical and physical properties of the samples were characterized using spectroscopic and diffractive methods. Bi_2S_3 samples were found to be in orthorhombic crystal structure while Fe_3O_4 samples were in a face-centred cubic (fcc) crystal form. The
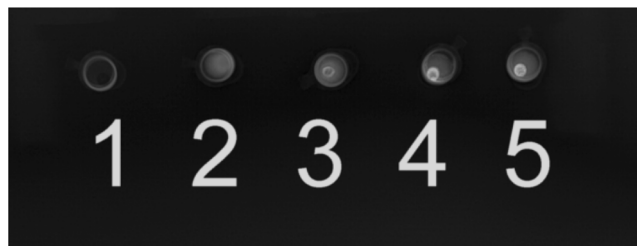
increased heat treatment does not change the crystal structure which was confirmed by XRD. XRD patterns also confirm that crystal structure was protected as the peaks observed in Bi_2S_3 and the peaks observed in Fe_3O_4 XRD patterns were also seen in the XRD pattern of $Bi_2S_3@Fe_3O_4$. Fe- and O-related peaks were seen in EDS spectra of Fe_3O_4 Bi, and S-related peaks were seen in the EDS spectra of Bi_2S_3 samples. Fe-, O-, Bi- and S- related peaks were seen in EDS spectra of $Bi_2S_3@Fe_3O_4$ where no contamination related peaks were observed. Further heat treatment enhances the size of Fe_3O_4 nanoparticles and also results in an alteration to the shape of Bi_2S_3 nanostructures. Magnetic properties of the samples were assessed using VSM Fe_3O_4 samples showing ferromagnetic behaviour. It was illustrated that the magnetic properties of the Bi_2S_3 samples were changed with doping nanostructures of Fe_3O_4 nanoparticles. The extended heat treatment augmented the magnetic saturation points of the sample. X-ray contrast agent properties of the samples were investigated using X-ray imaging. All the nanostructures produced possess X-ray contrast enhancement properties. Observations confirmed that nanoparticles may be considered a potential contrast agent to be used in medical applications. In addition, magnetic and photothermal properties of the nanocomposites may find a role in photothermal therapy and magnetic hyperthermia therapy applications.

Fig. 7 X-ray imaging of empty (1), water filled (2), Fe_3O_4+ water (3), Bi_2S_3 + water (4) and $Bi_2S_3@Fe_3O_4$ + water (5) Eppendorf tubes

References

1. Roduner, E.: Size matters: why nanomaterials are different (2006)
2. Koç, M.M., Aslan, N., Kao, A.P., Barber, A.H.: Evaluation of X-ray tomography contrast agents: a review of production, protocols, and biological applications. Microsc. Res. Tech. **82**, 812–848 (2019). https://doi.org/10.1002/jemt.23225
3. Ferrando, R., Jellinek, J., Johnston, R.L.: Nanoalloys: from theory to applications of alloy clusters and nanoparticles. Chem. Rev. **108**, 845–910 (2008). https://doi.org/10.1021/cr040090g
4. Johnston, R.L.: Atomic and molecular clusters (2002)
5. Kurban, H., Kurban, M., Dalkılıç, M.: Density-functional tight-binding approach for the structural analysis and electronic structure of copper hydride metallic nanoparticles. Mater. Today Commun. **21**, 100648 (2019). https://doi.org/10.1016/j.mtcomm.2019.100648
6. Kurban, M., Barış Malcıoğlu, O., Erkoç, Ş.: Structural and thermal properties of Cd–Zn–Te ternary nanoparticles: molecular-dynamics simulations. Chem. Phys. **464**, 40–45 (2016). https://doi.org/10.1016/J.CHEMPHYS.2015.11.003
7. Kurban, M.: Electronic structure, optical and structural properties of Si, Ni, B and N-doped a carbon nanotube: DFT study. Optik (Stuttg). **172**(295–301), 295 (2018). https://doi.org/10.1016/j.ijleo.2018.07.028
8. Köylüoğlu, B., Alaei, S., Kurban, M.: Molecular dynamics study on composition and temperature dependences of mechanical properties of CdTeSe nanowires under uniaxial stretching. Int. J. Mod.

Phys. B. **33**, 1950373 (2019). https://doi.org/10.1142/S0217979219503739

9. KURBAN, M.: Size- and composition-dependent structure of ternary Cd-Te-Se nanoparticles. Turk. J. Phys. **42**, 443–454 (2018)

10. Shipway, A.N., Katz, E., Willner, I.: Nanoparticle arrays on surfaces for electronic, optical, and sensor applications. Chemphyschem. **1**, 18–52 (2000). https://doi.org/10.1002/1439-7641(20000804)1:1<18::AID-CPHC18>3.0.CO;2-L

11. Xia, A., Chen, M., Gao, Y., Wu, D., Feng, W., Li, F.: Gd3+ complex-modified NaLuF4-based upconversion nanophosphors for trimodality imaging of NIR-to-NIR upconversion luminescence, X-Ray computed tomography and magnetic resonance. Biomaterials. **33**, 5394–5405 (2012). https://doi.org/10.1016/J.BIOMATERIALS.2012.04.025

12. Sun, Y.-F., Liu, S.-B., Meng, F.-L., Liu, J.-Y., Jin, Z., Kong, L.-T., Liu, J.-H., Sun, Y.-F., Liu, S.-B., Meng, F.-L., Liu, J.-Y., Jin, Z., Kong, L.-T., Liu, J.-H.: Metal oxide nanostructures and their gas sensing properties: a review. Sensors. **12**, 2610–2631 (2012). https://doi.org/10.3390/s120302610

13. Sathya Raj, D., Krishnakumar, T., Jayaprakash, R., Prakash, T., Leonardi, G., Neri, G.: CO sensing characteristics of hexagonal-shaped CdO nanostructures prepared by microwave irradiation. Sensors Actuators B Chem. **171–172**, 853–859 (2012). https://doi.org/10.1016/J.SNB.2012.05.083

14. Yakuphanoglu, F., Caglar, Y., Caglar, M., Ilican, S.: ZnO/p-Si heterojunction photodiode by solgel deposition of nanostructure n-ZnO film on p-Si substrate. Mater. Sci. Semicond. Process. **13**, 137–140 (2010). https://doi.org/10.1016/j.mssp.2010.05.005

15. Ameen, B.A.H., Yildiz, A., Farooq, W.A., Yakuphanoglu, F.: Solar light photodetectors based on nanocrystalline zinc oxide cadmium doped/p-Si heterojunctions. Silicon. **11**, 563–571 (2019). https://doi.org/10.1007/s12633-017-9656-4

16. Gupta, R.K.K., Yakuphanoglu, F., Amanullah, F.M.M.: Band gap engineering of nanostructure Cu doped CdO films. **43**, 1666–1668 (2011)

17. Aydın, C., Al-Hartomy, O.A., Al-Ghamdi, A.A., Al-Hazmi, F., Yahia, I.S., El-Tantawy, F., Yakuphanoglu, F.: Controlling of crystal size and optical band gap of CdO nanopowder semiconductors by low and high Fe contents. J. Electroceram. **29**, 155–162 (2012). https://doi.org/10.1007/s10832-012-9748-x

18. Yakuphanoglu, F., Aslam Farooq, W.: Photoresponse and electrical characterization of photodiode based nanofibers ZnO and Si. Mater. Sci. Semicond. Process. **14**, 207–211 (2011). https://doi.org/10.1016/j.mssp.2011.02.017

19. Yakuphanoglu, F.: Transparent metal oxide films based sensors for solar tracking applications. Compos. Part B Eng. **92**, 151–159 (2016). https://doi.org/10.1016/j.compositesb.2016.02.039

20. Rajput, J.K., Pathak, T.K., Kumar, V., Purohit, L.P.: Influence of sol concentration on CdO nanostructure with gas sensing application. Appl. Surf. Sci. **409**, 8–16 (2017). https://doi.org/10.1016/J.APSUSC.2017.03.019

21. Walsh, M.J., Yoshida, K., Kuwabara, A., Pay, M.L., Gai, P.L., Boyes, E.D.: On the structural origin of the catalytic properties of inherently strained ultrasmall decahedral gold nanoparticles. Nano Lett. **12**, 2027–2031 (2012). https://doi.org/10.1021/nl300067q

22. Chen, M., Kang, H., Gong, Y., Guo, J., Zhang, H., Liu, R.: Bacterial cellulose supported gold nanoparticles with excellent catalytic properties. ACS Appl. Mater. Interfaces. **7**, 21717–21726 (2015). https://doi.org/10.1021/acsami.5b07150

23. Sun, X., Frey Huls, N., Sigdel, A., Sun, S.: Tuning exchange bias in Core/Shell FeO/Fe3O4 nanoparticles. Nano Lett. **12**, 246–251 (2012). https://doi.org/10.1021/nl2034514

24. Liu, H., Sun, K., Zhao, J., Guo, R., Shen, M., Cao, X.: Dendrimer-mediated synthesis and shape evolution of gold–silver alloy nanoparticles. Colloids Surf. A Physicochem. Eng. Asp. 22–29 (2012)

25. Guo, R., Fang, L., Dong, W., Zheng, F., Shen, M.: Enhanced photocatalytic activity and ferromagnetism in Gd doped BiFeO3 nanoparticles. J. Phys. Chem. C. **114**, 21390–21396 (2010). https://doi.org/10.1021/jp104660a

26. Zhang, L., Xue, D., Gao, C.: Anomalous magnetic properties of antiferromagnetic CoO nanoparticles. J. Magn. Magn. Mater. **267**, 111–114 (2003). https://doi.org/10.1016/S0304-8853(03)00343-3

27. Ghosh, M., Sampathkumaran, E.V., Rao, C.N.R.: Synthesis and magnetic properties of CoO nanoparticles. Chem. Mater. **17**, 2348–2352 (2005). https://doi.org/10.1021/cm0478475

28. Djabri, A., Mahdi, M., Boukhalfa, R., Erkovan, M., Chumakov, Y., Chemam, F.: Structural, magnetic, and magneto-optical properties of Fe/cu superlattices. J. Supercond. Nov. Magn. **30**, 3207–3214 (2017). https://doi.org/10.1007/s10948-017-4128-z

29. Değer, C., Aköz, M.E., Erkovan, M., Yıldız, F.: Investigation on magnetic properties of soft/hard magnetic bilayers at different temperatures: a Monte-Carlo study. Acta Phys. Pol. A. **129**, 869–871 (2016). https://doi.org/10.12693/APhysPolA.129.869

30. Wang, Y., Wei, W., Li, F., Huang, B., Dai, Y.: Janus Bi2XYZ monolayers for light harvesting and energy conversion from first-principles calculations. Phys. E Low-Dimensional Syst. Nanostructures. **117**, 113823 (2020). https://doi.org/10.1016/j.physe.2019.113823

31. Chao, J., Xing, S., Liu, Z., Zhang, X., Zhao, Y., Zhao, L., Fan, Q.: Large-scale synthesis of Bi2S3 nanorods and nanoflowers for flexible near-infrared laser detectors and visible light photodetectors. Mater. Res. Bull. **98**, 194–199 (2018). https://doi.org/10.1016/j.materresbull.2017.10.026

32. Torrisi, L., Silipigni, L., Restuccia, N., Cuzzocrea, S., Cutroneo, M., Barreca, F., Fazio, B., Di Marco, G., Guglielmino, S.: Laser-generated bismuth nanoparticles for applications in imaging and radiotherapy. J. Phys. Chem. Solids. **119**, 62–70 (2018). https://doi.org/10.1016/J.JPCS.2018.03.034

33. Kinsella, J.M., Jimenez, R.E., Karmali, P.P., Rush, A.M., Kotamraju, V.R., Gianneschi, N.C., Ruoslahti, E., Stupack, D., Sailor, M.J.: X-ray computed tomography imaging of breast cancer by using targeted peptide-labeled bismuth sulfide nanoparticles. Angew. Chem. Int. Ed. **50**, 12308–12311 (2011). https://doi.org/10.1002/anie.201104507

34. Liu, J., Zheng, X., Yan, L., Zhou, L., Tian, G., Yin, W., Wang, L., Liu, Y., Hu, Z., Gu, Z., Chen, C., Zhao, Y.: Bismuth sulfide nanorods as a precision nanomedicine for in vivo multimodal imaging-guided photothermal therapy of tumor. ACS Nano. **9**, 696–707 (2015). https://doi.org/10.1021/nn506137n

35. Zhu, X., Zhou, J., Chen, M., Shi, M., Feng, W., Li, F.: Core–shell Fe3O4@ NaLuF4: Yb, Er/tm nanostructure for MRI, CT and upconversion luminescence tri-modality imaging. Biomaterials. **18**, 4618–4627 (2012)

36. Fattahi, H., Arsalani, N., Nazarpoor, M.: Synthesis and characterization of PVP-functionalized superparamagnetic Fe3O4 nanoparticles as an MRI contrast agent. Express Polym Lett. **4**, 329–338 (2010). https://doi.org/10.3144/expresspolymlett.2010.42

37. Ninjbadgar, T., Brougham, D.F.: Epoxy ring opening phase transfer as a general route to water dispersible superparamagnetic Fe3O4 nanoparticles and their application as positive MRI contrast agents. Adv. Funct. Mater. **21**, 4769–4775 (2011). https://doi.org/10.1002/adfm.201101371

38. Zeng, J., Jing, L., Hou, Y., Jiao, M., Qiao, R., Jia, Q., Liu, C., Fang, F., Lei, H., Gao, M.: Anchoring group effects of surface ligands on magnetic properties of Fe3O4 nanoparticles: towards high performance MRI contrast agents. Adv. Mater. **26**, 2694–2698 (2014). https://doi.org/10.1002/adma.201304744

39. Aktaş, S., Thornton, S.C., Binns, C., Lari, L., Pratt, A., Kröger, R., Horsfield, M.A.: Control of gas phase nanoparticle shape and its effect on MRI relaxivity. Mater. Res. Express. **2**, (2015). https://doi.org/10.1088/2053-1591/2/3/035002

40. Aktas, S., Thornton, S.C., Binns, C., Denby, P.: Gas phase synthesis of core-shell Fe@FeOx magnetic nanoparticles into fluids. J. Nanopart. Res. **18**, (2016). https://doi.org/10.1007/s11051-016-3659-8

41. Binns, C., Prieto, P., Baker, S., Howes, P., Dondi, R., Burley, G., Lari, L., Kröger, R., Pratt, A., Aktas, S., Mellon, J.K.: Preparation of hydrosol suspensions of elemental and core-shell nanoparticles by co-deposition with water vapour from the gas-phase in ultra-high vacuum conditions. J. Nanopart. Res. **14**, (2012). https://doi.org/10.1007/s11051-012-1136-6

42. Feng, W., Zhou, X., Nie, W., Chen, L., Qiu, K., Zhang, Y., He, C.: Au/polypyrrole@Fe3O4 nanocomposites for MR/CT dual-modal imaging guided-photothermal therapy: an n vitro study. ACS Appl. Mater. Interfaces. **7**, 4354–4367 (2015). https://doi.org/10.1021/am508837v

43. Kolen'ko, Y.V., Bañobre-López, M., Rodríguez-Abreu, C., Carbó-Argibay, E., Sailsman, A., Piñeiro-Redondo, Y., Cerqueira, M.F., Petrovykh, D.Y., Kovnir, K., Lebedev, O.I., Rivas, J.: Large-scale synthesis of colloidal Fe3O4 nanoparticles exhibiting high heating efficiency in magnetic hyperthermia. J. Phys. Chem. C. **118**, 8691–8701 (2014). https://doi.org/10.1021/jp500816u

44. Barick, K.C., Singh, S., Bahadur, D., Lawande, M.A., Patkar, D.P., Hassan, P.A.: Carboxyl decorated Fe3O4 nanoparticles for MRI diagnosis and localized hyperthermia. J. Colloid Interface Sci. **418**, 120–125 (2014). https://doi.org/10.1016/j.jcis.2013.11.076

45. Tran, L.D., Hoang, N.M.T., Mai, T.T., Tran, H.V., Nguyen, N.T., Tran, T.D., Do, M.H., Nguyen, Q.T., Pham, D.G., Ha, T.P., Van Le, H., Nguyen, P.X.: Nanosized magnetofluorescent Fe3O4-curcumin conjugate for multimodal monitoring and drug targeting. Colloids Surf. A Physicochem. Eng. Asp. **371**, 104–112 (2010). https://doi.org/10.1016/j.colsurfa.2010.09.011

46. Lei, W., Liu, Y., Si, X., Xu, J., Du, W., Yang, J., Zhou, T., Lin, J.: Synthesis and magnetic properties of octahedral Fe3O4 via a one-pot hydrothermal route, vol. 381, p. 314 (2017)

47. Tang, C., Wang, C., Su, F., Zang, C., Yang, Y., Zong, Z., Zhang, Y.: Controlled synthesis of urchin-like Bi2S3 via hydrothermal method. Solid State Sci. **12**, 1352–1356 (2010). https://doi.org/10.1016/j.solidstatesciences.2010.05.007

48. Sharma, S., Kumar, D., Khare, N.: Plasmonic Ag nanoparticles decorated Bi 2 S 3 nanorods and nanoflowers: their comparative assessment for photoelectrochemical water splitting. Int. J. Hydrog. Energy. **44**, 3538–3552 (2019). https://doi.org/10.1016/j.ijhydene.2018.11.238

49. Zhu, H., Jiang, R., Li, J., Fu, Y., Jiang, S., Yao, J.: Magnetically recyclable Fe3O4/Bi2S3 microspheres for effective removal of Congo red dye by simultaneous adsorption and photocatalytic regeneration. Sep. Purif. Technol. **179**, 184–193 (2017). https://doi.org/10.1016/j.seppur.2016.12.051

50. Hong, R.Y., Zhang, S.Z., Di, G.Q., Li, H.Z., Zheng, Y., Ding, J., Wei, D.G.: Preparation, characterization and application of Fe3O4/ZnO core/shell magnetic nanoparticles. Mater. Res. Bull. **43**, 2457–2468 (2008). https://doi.org/10.1016/j.materresbull.2007.07.035

51. Qu, F., Wang, Y., Liu, J., Wen, S., Chen, Y., Ruan, S.: Fe3O4-NiO core-shell composites: hydrothermal synthesis and toluene sensing properties. Mater. Lett. **132**, 167–170 (2014). https://doi.org/10.1016/j.matlet.2014.06.060

52. Sharma, S., Khare, N.: Hierarchical Bi2S3 nanoflowers: a novel photocatalyst for enhanced photocatalytic degradation of binary mixture of Rhodamine B and Methylene blue dyes and degradation of mixture of p-nitrophenol and p-chlorophenol. Adv. Powder Technol. **29**, 3336–3347 (2018). https://doi.org/10.1016/j.apt.2018.09.012

53. Prozorov, T., Kataby, G., Prozorov, R., Gedanken, A.: Effect of surfactant concentration on the size of coated ferromagnetic nanoparticles. Thin Solid Films. **340**, 189–193 (1999). https://doi.org/10.1016/S0040-6090(98)01400-X

54. Reddy, K.R., Lee, K.P., Gopalan, A.I.: Novel electrically conductive and ferromagnetic composites of poly(aniline-co-aminonaphthalenesulfonic acid) with iron oxide nanoparticles: synthesis and characterization. J. Appl. Polym. Sci. **106**, 1181–1191 (2007). https://doi.org/10.1002/app.26601

55. Dutz, S., Hergt, R., Mürbe, J., Müller, R., Zeisberger, M., Andrä, W., Töpfer, J., Bellemann, M.E.: Hysteresis losses of magnetic nanoparticle powders in the single domain size range. J. Magn. Magn. Mater. **308**, 305–312 (2007). https://doi.org/10.1016/j.jmmm.2006.06.005

56. Xu, X., Xu, C., Dai, J., Hu, J., Li, F., Zhang, S.: Size dependence of defect-induced room temperature ferromagnetism in undoped ZnO nanoparticles. J. Phys. Chem. C. **116**, 8813–8818 (2012). https://doi.org/10.1021/jp3014749

57. Keng, P.Y., Bull, M.M., Shim, I.B., Nebesny, K.G., Armstrong, N.R., Sung, Y., Char, K., Pyun, J.: Colloidal polymerization of polymer-coated ferromagnetic cobalt nanoparticles into Pt-Co3O4 nanowires. Chem. Mater. **23**, 1120–1129 (2011). https://doi.org/10.1021/cm102319d